Properties of TiSiN coatings deposited by hybrid HiPIMS and pulsed-DC magnetron co-sputtering

Mohammad Arab Pour Yazdi, F. Lomello, J. Wang, Frédéric Sanchette, Z. Dong, T. White, Y. Wouters, F. Schuster, Alain Billard

Properties of TiSiN coatings deposited by hybrid HiPIMS and pulsed-DC magnetron co-sputtering

M. Arab Pour Yazdi [a, *], F. Lomello [b, c], J. Wang [c, d, f], F. Sanchette [e], Z. Dong [d], T. White [d], Y. Wouters [f], F. Schuster [b], A. Billard [a, c]

[a] *IRTES-LERMPS-UTBM, site de Montbéliard, 90010 Belfort cedex, France*
[b] *CEA Cross-Cutting Program on Advanced Materials Saclay, 91191 Gif-sur-Yvette, France*
[c] *LRC CEA-UTBM LIS-HP, site de Montbéliard, 90010 Belfort cedex, France*
[d] *School of Materials Science and Engineering, Nanyang Technological University, 50 Nanyang Avenue, Singapore 639796, Singapore*
[e] *Institut Charles Delaunay, Laboratoire des Systèmes Mécaniques et d'Ingénierie Simultanée – UMR CNRS 6281, LRC NICCI, CEA-ICD-LASMIS-UTT, UTT, Antenne de Nogent-52, Pôle Technologique de Haute-Champagne, 52800 Nogent, France*
[f] *SiMaP, UMR CNRS/UJF/Grenoble INP, 1130 rue de la Piscine, BP 75, 38402 Saint-Martin d'Hères Cedex, France*

TiSiN nanocomposites coatings were synthesized for the first time by a hybrid deposition technique where high power impulse (HiPIMS) and pulsed-DC (PDCMS) magnetron co-sputtering were used for Ti and Si deposition respectively in an Ar + N_2 atmosphere. For the Ti target, the deposition parameters were fixed, while the current applied to the Si target ranged from 0 to 0.9 A. Thus, the Si content in the films was adjusted from 0 to 8.8 at.% Si to allows tailoring of microstructure and mechanical properties. TiSiN grain sizes decreased from ~41 to ~6 nm as the coatings became more siliceous. The hardness increased from 20 ± 0.41 to 41.31 ± 2.93 GPa when the Si concentration rose from 0 to 4.4 at.% Si, but beyond this last value, hardness degrades reaching 36.1 ± 2.21 GPa at 8.8 at.% Si. The wear behaviours evaluated by ball-on-disc tests were correlated with the Hardness/Young's modulus ratio. Moreover, the silicon enhanced the oxidation resistance and the least hardness deterioration was found in the sample with the higher silicon content (8.8 at.% Si) after a thermal annealing in air (2 h/700 °C).

1. Introduction

Since the early 1980s, many methods have been developed for processing titanium–silicon nitride nanocomposites including plasma enhanced chemical vapour deposition (PECVD), magnetron sputtering, cathodic arc (PVD) and/or large area filtered arc deposition (LAFAD) that create coatings with interesting enhanced mechanical properties compared to single-phase titanium nitride [1,2]. In this context, PVD and LAFAD are especially advantageous since they avoid the precursor gases that prove inconvenient with respect to corrosion, fire and environmental hazards.

Superhard TiSiN coatings (>40 GPa) show many advantages such as high toughness and thermal stability up to 800 °C in an air atmosphere [1]. *Vepřek* et al. showed that by increasing the Si content up to ≈8–9 at.% Si limits the TiN nanocrystallites growth to 3–3.5 nm with superior mechanical properties (≈50 GPa) in samples processed by PECVD [3]. Over a threshold, highly siliceous coatings show degraded mechanical properties. Nonetheless, Si addition improves the oxidation resistance of TiN based coatings due to SiO_2 shielding the TiN nanocrystallites [1,4].

The nanocomposites processed by PECVD present a biphased microstructure composed of nanocrystalline TiN grains embedded in a hard amorphous a-Si_3N_4 phase [5]. Such microstructures can only arise because PECVD ensures fast diffusion driven by a high ion energy and/or temperature that allows phase segregation [6]. In contrast, low-temperature PVD (<300 °C) processes generally favour the production of metastable solid solutions of TiSiN [7,8]. This phenomenon was also reported by *Schmitt* et al. for the CrSiN system in which the Si content influences the microstructure development, evolving from a solid solution to a biphasic nanocomposite [9]. As a matter of fact, these nanocomposites, with a higher Si content, exhibit two different Si concentration zones.

In this study, TiSiN coatings were produced by means of high power impulse (HiPIMS) coupled with DC-pulsed magnetron sputtering (PDCMS) techniques. The former supplied the power to

* Corresponding author. Tel.: +33 384 58 37 33.
E-mail addresses: arabpour121@yahoo.fr, mohammad.arab-pour-yazdi@utbm.fr (M. Arab Pour Yazdi).

the Ti target. HiPIMS discharge operates with peak power densities (>0.5 kW/cm^2) which provoke the ionization of a large fraction of the sputtered atoms as described in several previous studies [10]. Firstly, this phenomenon enables the metal ion implantation at the substrate-coating interface during etching, thus improving the film adhesion [11]. Secondly, during the film deposition, an efficient ion bombardment enhances the adatom mobility on the surface thus enabling the production of denser coatings [11].

In this novel approach, HiPIMS and PDCMS allowed the production of similar coatings in terms of mechanical properties and adhesion compared with cathodic arc deposition (CAD) with an improved morphology [12]. Indeed, since magnetron sputtering techniques (MS) were employed, the coatings exhibit an absence of macro-droplets which are the responsible for increasing the coating roughness in CAD [13].

The motivation for preparing these nanocomposites arises from their nanosafe-by-design character, since they fabricated in a one-step *in-situ* process without nanoparticles handling [14]. In this study, the hybrid technique was employed for producing TiSiN coatings for the first time following as already reported for different nitride systems [15–18]. On one hand, the PDCMS applied to Si target permitted to obtain higher deposition rates and better control of Si content in the coatings. On the other hand, HiPIMS allowed to enhance the densification and adhesion of the coating compared to classical techniques. The properties evolution of TiSiN samples having different Si content was established. The latter was based on the mechanical-tribological characterization, as well as, the thermal stability up to 700 °C in air was also highlighted.

2. Material and methods

Two Ti- and Si-targets (99.9% purity – 128 × 254 mm^2) were employed simultaneously in a Balzers 640 R unit. On one hand, the former was powered by a HiPIMS (Hüttinger 4002) generator employing the following parameters: $U_{peak} = -700$ V, $T_{on} = 28$ μs, duty cycle = 0.14%, f = 500 Hz, peak discharge current of $I_{peak} = 142$ A and average current of $I_{ave} \approx 2$ A. On the other hand, with the aim of varying the silicon content, the Si-sputtering was conducted by pulsed-DC (Pinnacle Plus, Advanced Energy) in the 0 → 0.9 A (<200 W) range average current (I_{ave}), a $T_{off} = 5$ μs and a $f = 50$ kHz. The rotating substrate holder was fixed at a constant speed of ≈20 revolutions per minute (r.p.m.). A schematic illustration of the PVD device is shown in Fig. 1. In this study, mirror polished AISI M2 HSS cylindrical substrates (63 HRc, ∅ = 30 mm) were employed. These substrates were degreased in alcohol before deposition. The morphology of the fractured surfaces was characterized by means of a Thermal Field Emission Scanning Electron Microscope (FE-SEM JEOL JSM-7800F). Three specimens were examined by Transmission Electron microscopy (TEM JEOL JEM-2100F) operated at 200 kV.

The Si content was measured by energy dispersive X-ray spectroscopy (EDS) with a precision of ±0.5% inherent to the technique employed. The X-ray diffraction (XRD) before and after thermal annealing was performed by means of XRD Brüker D8 Focus device in a θ–2θ mode ($\lambda_{K\alpha 1+\alpha 2\ Co} = 0.1788970$ nm). The XRD analysis allowed the calculation of the crystallites mean size by applying the Debye-Scherrer method [19].

Hardness and the effective Young's modulus $E^* = E/(1-\nu^2)$ – where E and ν are the Young's modulus and Poisson ratio respectively – of coatings were measured by means of a nanohardness tester (NHT CSM Instruments) using a Berkovich diamond tip from loading/unloading curves. The Oliver and Pharr method [20] was employed. Final values and errors were calculated from an average of 40 indentations with imposed penetration depths shallower than 10% of the coatings thickness, according to the Bückle's rule

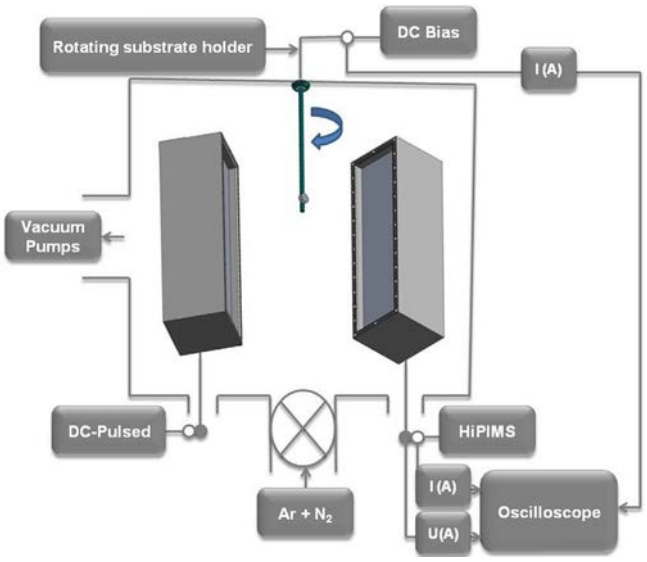

Fig. 1. Schematic illustration of the PVD device employed in this study.

[21]. Young's modulus values could be overestimated because of the substrate influence on thin film elastic response for relative indentation depth above 1–2% of coating thickness [22].

Ball-on-disc tests were performed by using a CSM tribometer. As counter material, WC/Co balls of 6 mm diameter was employed. The tribological tests were conducted following fixed conditions: in air, a constant load of 10 N, a wear track nominal diameter of 6 mm, a sliding velocity of 100 mm s^{-1}over a sliding distance of 600 m, a relative humidity between 33 and 39% RH and temperature range (19–22 °C).

A white-light profilometer (ALTISURF500) allowed quantifying the wear after ball-on-disc tests at four different areas. The resolution is 10 nm on the height measurements (z-height), while its spatial resolution is 0.5 μm (x direction). In the present study, the scanning speed was fixed at 15 μm s^{-1}. Finally, the oxidation resistance tests were carried out in a dry air atmosphere at 700 °C with a dwell time of 2 h. During the thermal annealing, heating and cooling rates were 2 and 3 °C min^{-1}, respectively.

3. Results

3.1. Structure and composition analysis

In Fig. 2, the variation of elements content determined by energy dispersive X-ray spectroscopy (EDS) versus the Si target current (A) is presented. The Si content was tailored by increasing the applied current in the target. The Ti target parameters were fixed (Table 1) for all samples as well as the argon and nitrogen flows. By increasing the current applied on Si target up to 0.9 A, the Si concentration increased to about 8.8 at.% whereas Ti decreased progressively from 48.5 down to 35.9 at.%. Both N and C contents remained stable at around 50.7 and 2.54 at.%, respectively. As reported by *Ehiasarian* et al., the voided grain boundaries on the surface permit to incorporate carbon and oxygen in (1 1 1) textured coatings [23]. Precisely, oxygen and argon levels were lower than 1 at.%.

X-ray diffraction patterns of the TiSiN films with silicon content varying from 0 to 8.8 at.% Si are presented in Fig. 3. The increase of silicon concentration induced an evolution of the preferential orientation. The TiN crystalline structure matches with the NaCl–B1 face-centred cubic (FCC) type structure (JCDD cards # 03-

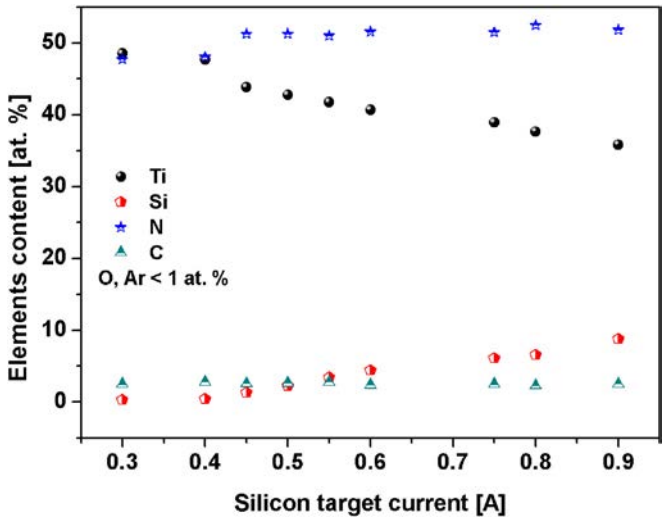

Fig. 2. EDS quantitative analysis as a function of the Si target current (A).

065-5759) with a strong preferential orientation with the (111) plans parallel to the substrate surface. This preferential orientation is commonly found after certain thickness range and/or when deposition flux is characterized by low ion (gas)-to-metal (neutral) ratio [23]. While the silicon content increased up to 2.3 at.% Si, as reported in several studies, the texture evolves into a (2 0 0) orientation followed by the slight peak broadening. The increase of the silicon content over 1.3 at.% Si leads to extinction of (1 1 1) orientation since random orientated nanocrystallites are formed in agreement with *Patscheider* et al. [24]. The texture evolution is commonly ascribed to the surface energy [25]. When the number of atoms inside the nanocrystallites is reduced, the surface free energy is progressively increased. In order to counteract this phenomenon, the nanocrystallites are able to reduce their free energy by changing their preferential orientation.

As reviewed in literature, at higher silicon content >8 at.% Si, an upper supersaturation appears giving broad diffraction peaks [5,26]. Indeed, almost only M2 substrate peaks were observed.

Table 1
Deposition parameters.

Titanium target	
HiPIMS generator	Hüttinger 4002
Maximum peak voltage	−700 V
Maximum target current	≈142 A ($I_{Ave.} \leq$ 2 A)
Maximum average power	≤1.4 KW
Pulse time T_{on}	28 μs
Duty cycle (%)	0.14
Frequency	500 Hz
Drawing distance (mm)	50
Silicon target	
Pulsed-DC generator	Pinnacle plus, advanced energy
Average target current (I_{AVE})	0 → 0.9 A
Maximum power	<200 W
T_{off}	5 μs
Frequency	50 kHz
Drawing distance (mm)	140
Total pressure	~0.5 Pa
Ar flow rate	200 sccm
N_2 flow rate	5 sccm
Substrates	M2 HSS, 63HRc
Bias voltage	−50 V
Rotation speed	≈20 r.p.m.
Deposition temperature	<200 °C
Deposition time	180 min

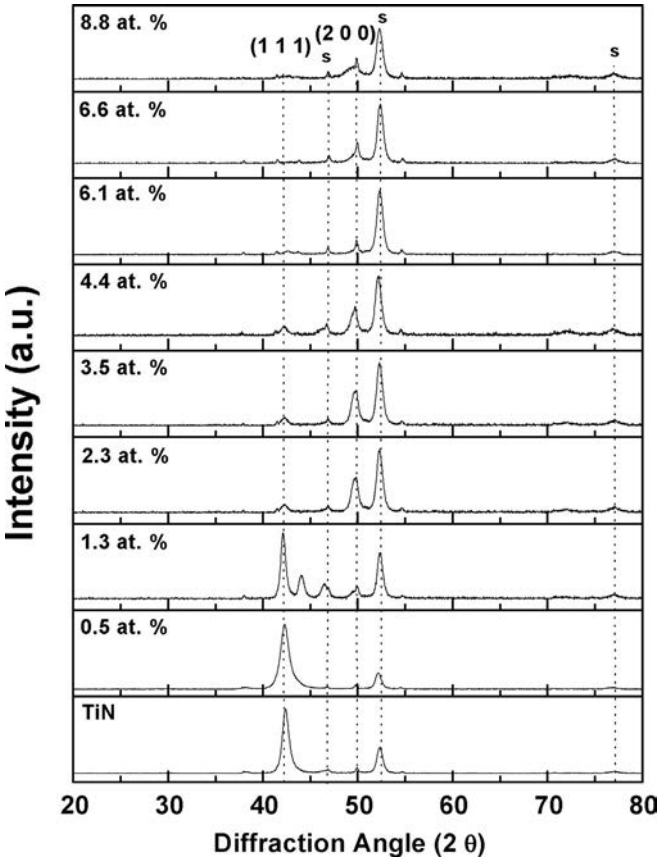

Fig. 3. X-ray diffraction patterns of the as-deposited films as a function of the Si content ("s" = indexes the substrate peaks).

The lattice parameter evolution was calculated from the average peak positions of (1 1 1) and (2 0 0) from XRD data according to the Bragg's law. As shown in Fig. 4, the lattice parameter evolved associated with the structure change from a solid solution to a nanocomposite structure as reported for the CrSiN system by *Schmitt* et al. [9]. In fact, in the first stage, up to 3.5 at.% Si, the lattice parameter diminished progressively from 0.4253 nm a value closer to the nominal lattice parameter a_o = 0.425 nm − to 0.4241 nm. Over 3.5 at.% Si of silicon content, the second stage, the lattice

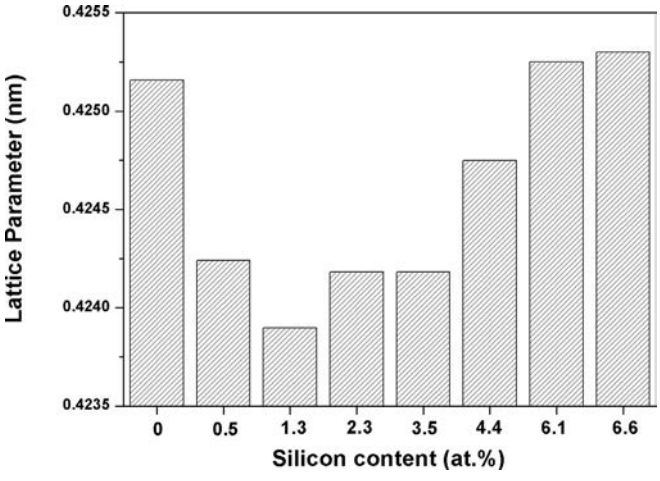

Fig. 4. Lattice parameter evolution as a function of the silicon content.

parameter increased up to a closer value compared to the a_0, i.e. 0.42475 nm at 4.4 at.% Si. According to the literature, the lattice reduction in the first stage (up to 3 at.% Si) is imputed to the solid solution formation. In this stage, the Si atoms are introduced progressively in the TiN cubic lattice. Since the smaller Si atoms occupy the Ti positions replacing them, they induce a reduction in the lattice parameter.

On the contrary, over the saturation threshold (p_c), the formation of a second phase TiSiN amorphous matrix richer in silicon occurs, and as a consequence, it allows the formation of the expected nanocomposite structure. The crystalline phase is then desaturated and the lattice parameter increases.

Firstly, the Si allows the solid solution formation replacing the Ti atoms in the lattice and secondly, over a saturation threshold (p_c), the amorphous phase is formed embedding the TiSiN nanocrystallites. The transition was observed near 3.5 at.% Si content. This phenomenon was accompanied by the lattice parameter increasing tendency as reported *Schmitt* et al. [9].

3.2. Grain size

In Fig. 5, the mean sizes of TiN crystallites of the TiSiN coatings as a function of the silicon content variation from 0 to 8.8 at.% Si are presented and compared to those found in the literature. The crystallite size evolved from ≈41 nm in the single TiN to ≈6 nm in the nanocomposite when silicon content increased up to 8.8 at.% Si. A similar trend was reported in literature for the same type of nanocomposites [5,24]. As reported by several authors, the decrease of TiN crystallites size inside the SiN_x matrix can be divided into three zones [5,24]. The first zone (up to 1.3 at.% Si) is characterized by a rapid reduction of grain size from 40.8 ± 0.3 to 12.87 ± 0.1 nm ascribed to silicon enrichment. An augmentation in Si content (above 1.3 at.% Si) promoted the transition between the solid solution and the nanocomposite structure. This phenomenon is ascribed to the saturation in relation to the Si substitution as well as the TiN nanocrystallites encapsulation as a function of the amorphous phase enrichment during film growth. The 2nd zone is generally accompanied by texture evolution from (1 1 1) to (2 0 0) as observed in the XRD patterns (Fig. 3). The consequence is the stabilization of the TiN grain size (6.36 ± 0.22 nm) in the 2nd zone when Si contents range from 1.3 to 4.4 at.% Si. Over 4.4 at.% of Si content, a constant TiN average crystallite size value near 5 nm was measured.

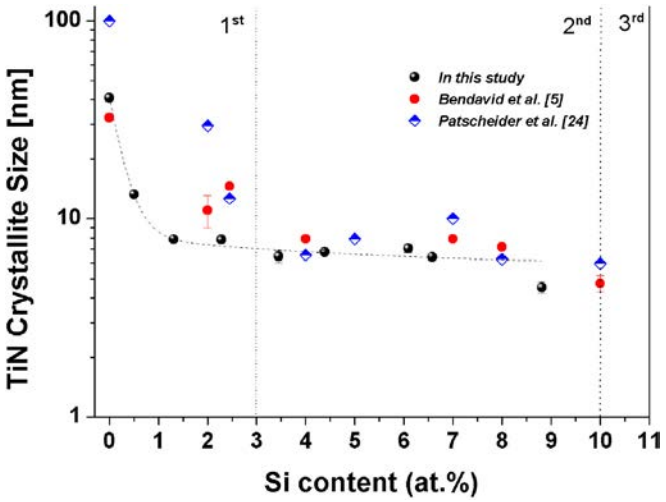

Fig. 5. Dependence of the grain size on the silicon content.

3.3. Structure & morphology

On one hand, the cross-section micrographs of TiN and TiSiN (4.4 at.%) fracture surfaces are shown in Fig. 6. Both coatings exhibit a dense morphology and thicknesses of about2.3 μm. Deposition rate in all coatings was about 0.76 μm/h.

On the other hand, TEM observation shows the microstructural evolution from solid solution to nanocomposite (Fig. 7). The micrographs reveal the continuous enrichment of the amorphous phase. It is supposed that in the 1st zone, up to a value near 1.3 at.%, silicon is essentially in solid solution. As shown in Fig. 7(A), the sample with 0.5 at.% Si corresponds to the 1st zone in which single nanocrystallites are clearly visible. In point of fact, it is believed that near 1.3 at.% of Si content, the transition into nanocomposite takes place, thus confirming the previous hypothesis. In contrast, by increasing the Si content, above 1.3 at.% upto 4.4 at.% Si, the microstructure evolved from the solid solution to a nanocomposite with distinct two phases - Fig. 7(B), as already reported by *Schmitt* et al. [9]. It is clearly visible that TiN nanocrystallites (dark-gray) are embedded and randomly (inhomogeneously) surrounded by a non-crystalline phase (light-gray). The average crystallite size is consistent (≈6 nm) with the values calculated by the Debye-Scherrer method. The measurement was quite complex since to the nanocrystallites superposition could alter the estimation. Nonetheless, it confirms the modification concerning the film growth mechanism. Finally, as shown in Fig. 7(C), the sample with the higher silicon content (8.8 at.% Si) is partially amorphous since few nanocrystallites were observed. In fact, the main TiN peak (2 0 0) is still present in the XRD pattern.

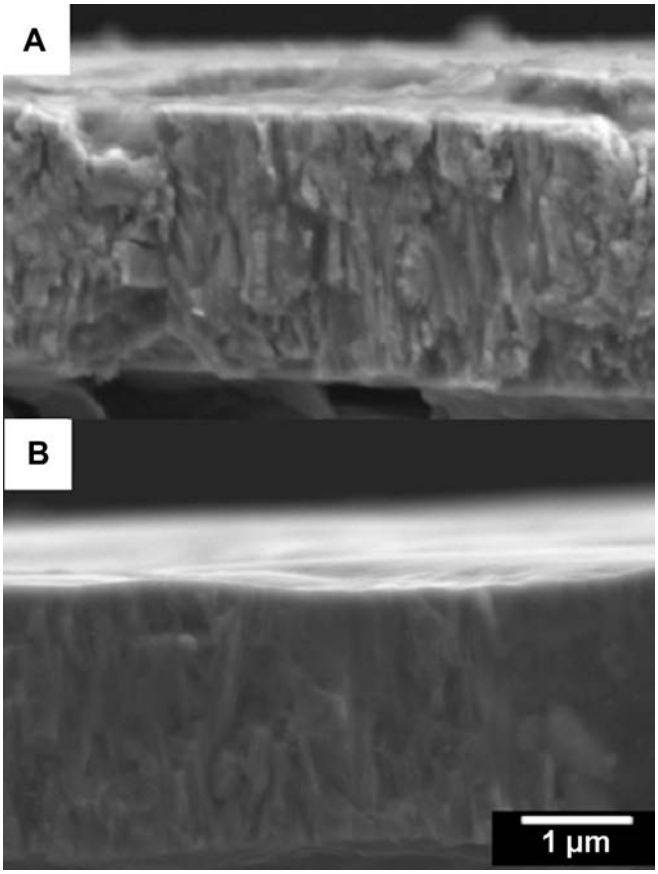

Fig. 6. FE-SEM cross-section micrograph (20 kx) of the coatings: (A) single TiN & (B) TiSiN with 4.4 at.% Si.

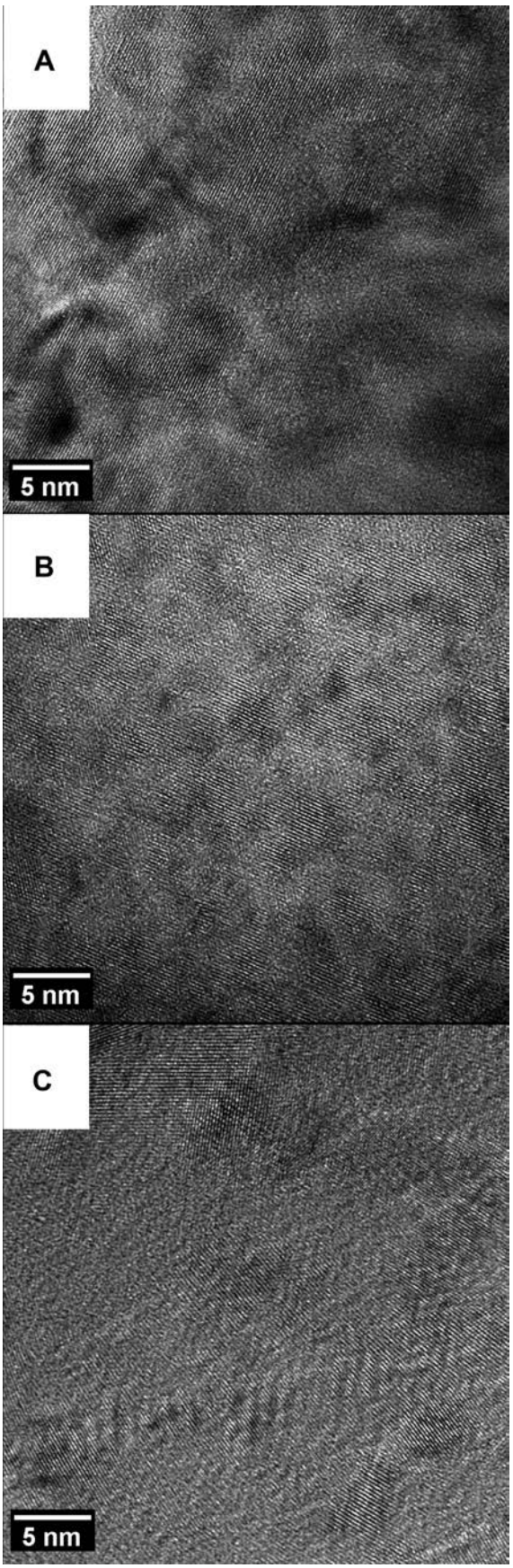

Fig. 7. HR-TEM micrographs of the TiSiN samples with (A) 0.5, (B) 4.4 & (C) 8.8 at.% Si.

Selected area electron diffraction (SAED) patterns of samples containing 0.5 and 4.4 at.% Si are shown in Fig. 8. The three diffraction rings corresponding to (1 1 1), (2 0 0) and (2 2 0) from the FCC-type structure are indexed. In Fig. 8(A) sample with 0.5 at.% Si exhibits brighter spots in the (1 1 1) preferred orientation following the film growth direction.

On the contrary, the sample with 4.4 at.% Si presented in Fig. 8(B) presents a (2 0 0) preferred orientation composed of discrete spots. In both cases, the SAED patterns are in perfect agreement with the X-ray diffraction patterns (Fig. 3).

3.4. Mechanical properties

Fig. 9 shows Young's modulus (E) and hardness (H) as a function of the Si content. A significant increase of hardness was measured when Si content is 3.5 at.% Si consistent with the solid solution hardening effect. These values are substantially higher compared to single-phase TiN 20 ± 0.41 GPa. The more pronounced hardness (H) enhancement 41.31 ± 2.93 GPa was measured in samples with 4.4 at.% Si associated with the grain size refinement (6.36 ± 0.22 nm) in the 2nd zone and the formation of the nanostructure which implies a high density of GBs as claimed by *Vepřek* [27].

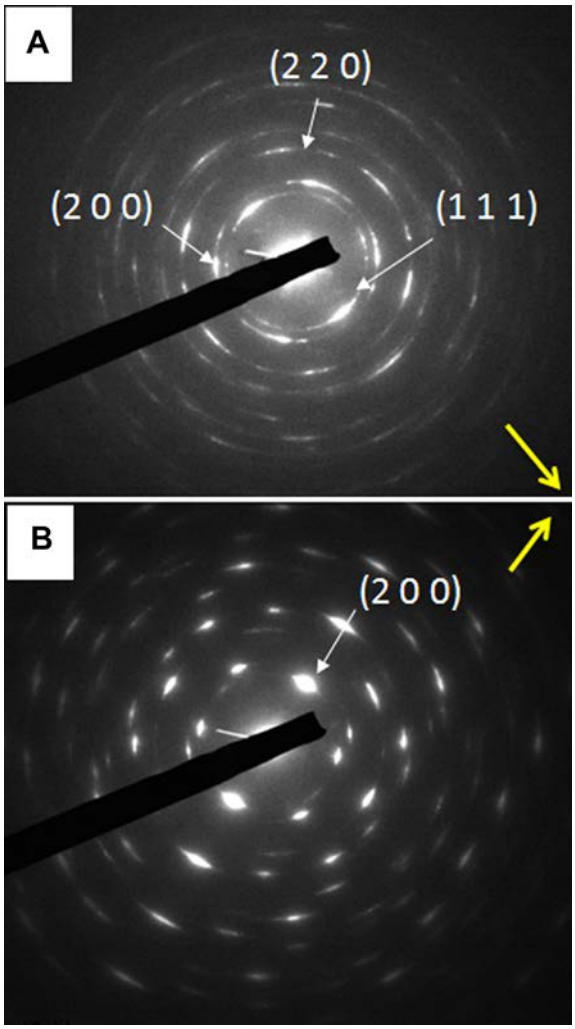

Fig. 8. Selected area electron diffraction (SAED) patterns from TiSiN samples with 0.5 and 4.4 at.% Si (the yellow arrow indicates the film growth direction). (For interpretation of the references to colour in this figure legend, the reader is referred to the web version of this article.)

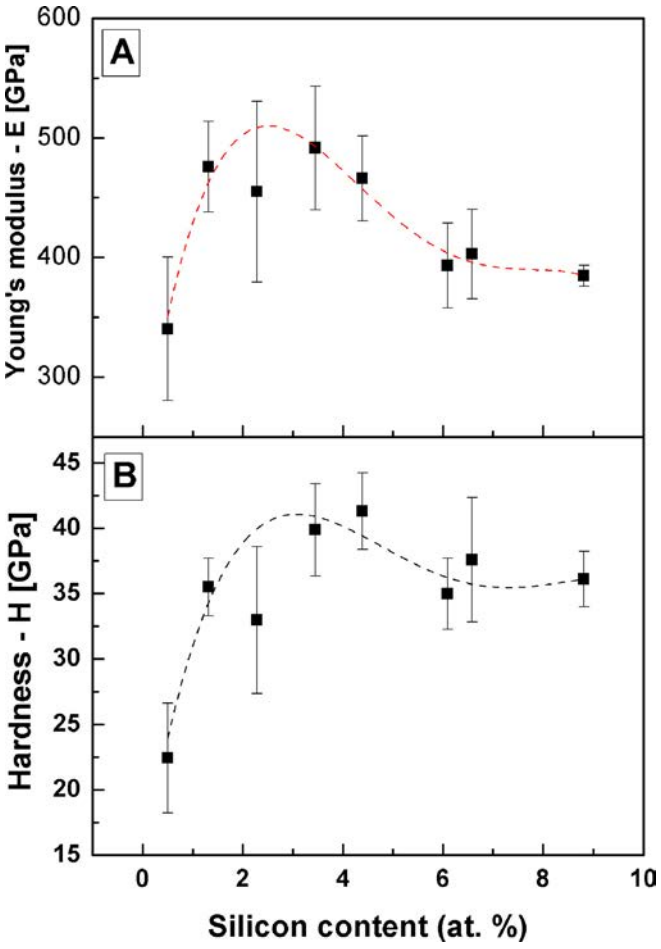

Fig. 9. (A) Young's modulus & (B) hardness as a function of Si content.

Over 4.4 at.% Si both hardness (H) and Young's modulus (E) slight decline down to 36.1 ± 2.21 GPa. The values did not decreased drastically since they belong to the 2nd zone. As described in the literature, over the certain percolation threshold (p_c) in the 3rd zone, a loss of the interaction between the two phases permits the crack propagation through the amorphous matrix [24]. This phenomenon provokes the decrease of hardness.

3.5. Tribological properties and wear behaviour

In Fig. 10(A), the evolution of the friction coefficient as a function of the sliding distance is shown. The friction coefficients presented similar values in 0.5 → 0.8 range at the steady state and a slight diminution of the friction coefficient was observed when the silicon content increased up to 4.4 at.% Si. As reviewed by several authors, this slight reduction in terms of the friction coefficient could be explained by the formation of the self-lubricant tribo-layers [28]. In these particular nanocomposites, SiO_2 and/or $Si(OH)_2$ is formed during wear tests at humid environments proportionally with the increasing silicon contents [29].

On the contrary, some fluctuation is observed during tribological tests when the sliding distance reaches 500 m. This behaviour could be ascribed to the debris produced during the tribological tests. These debris are supposed to remain in the local regions of the wear track, hence causing the variation with respect to the friction coefficient (instability) [30].

Similarly, the wear behaviour was correlated with the friction coefficient evolution. In Fig. 10(B) the wear scar profile of two samples is presented. The depth of wear tracks is inversely proportional to the mechanical properties evolution, being higher in single TiN. A similar trend was reported by *Cheng* et al. using ceramic balls as counter materials corresponding to abrasive wear [2]. It is well known that the wear behaviour strongly depends on the ratio between the mechanical properties of the counter materials and the coating [31].

As reviewed by *Leyland and Matthews*, the wear behaviour is usually determined by the H/E ratio [32,33]. For the sake of clarity, in this study, the dimensionless parameter was calculated for the three samples corresponding to the three zones (Fig. 11).

In fact, an increasing H/E parameter from 0.065 ± 0.0014 to 0.088 ± 0.0001 was obtained. These values are in good agreement with the apparent decreasing wear shown in Fig. 10(B).

A higher friction coefficient is usually ascribed to higher debris' generation on the wear track during ball-on-disc tests. However, no significant differences on the subject of the wear behaviour were found, probably ascribable to the tribological parameters (speed, load, etc.) and the counter material (WC/Co) employed in the present study.

3.6. Oxidation resistance

With the aim of evaluating the stability against oxidation, a 2 h annealing treatment at 700 °C was carried out in air. After oxidation, especially in case of single TiN, the XRD patterns show a mixture of TiO_2(rutile, JCDD cards # 01-087-0920), TiN and substrate peaks as shown in Fig. 12. The TiO_2-rutile is believed to be formed due to the progressive removal of N from TiN. This phenomenon was already reported in literature when the oxidation is carried out at >600 °C in an air atmosphere [4].

As a matter of fact, the oxidation resistance was enhanced by only increasing up to 4.4 at.% Si. This result is in good agreement

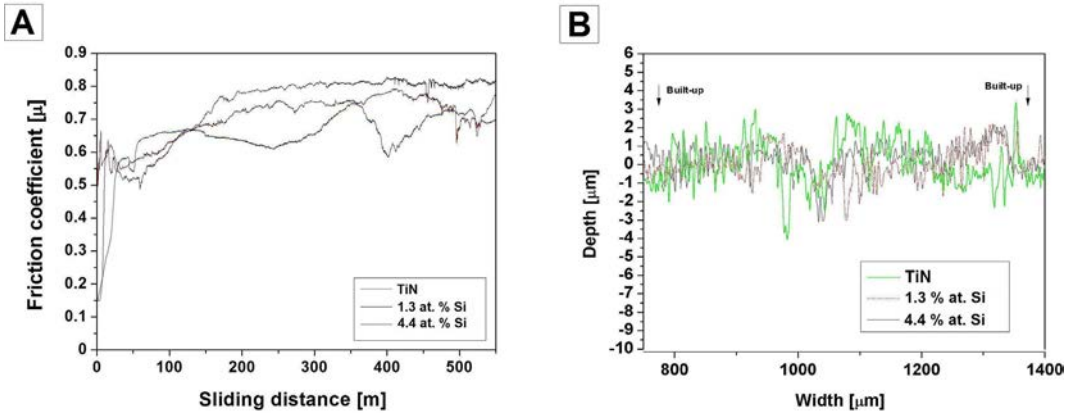

Fig. 10. (A) Coefficient of friction versus the sliding distance and (B) 2-D profile of the wear scar after ball-on-disc tests against WC/Co ball.

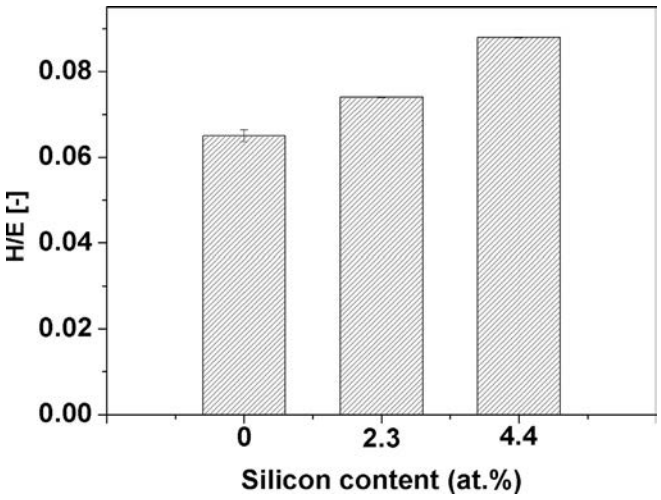

Fig. 11. Evolution of the *H*/*E* ratio as a function of the Si content.

with the *Diserens* et al. work [34].Subsequently, the TiO_2-rutile peaks' intensity was drastically reduced when the Si content was increased up to 4.4 at.% Si. Furthermore, no TiO_2-rutile was found in samples containing >6.6 at.% Si.

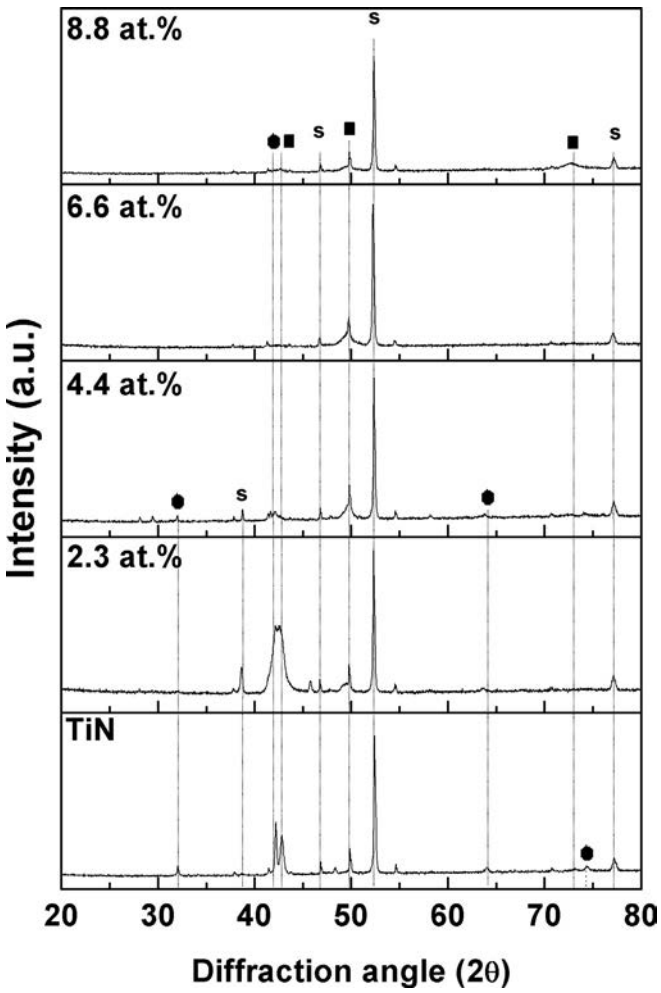

Fig. 12. X-ray diffraction patterns of the oxidized samples with different Si contents after thermal annealing (2 h/700 °C/air) (• = TiO_2-rutile, ■ = titanium nitride & s = substrate peaks).

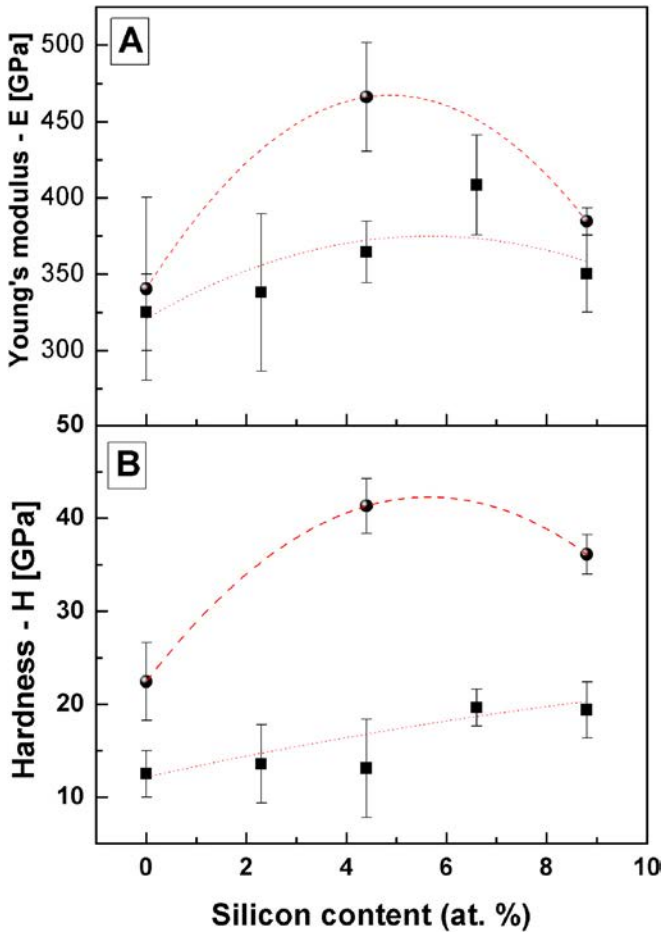

Fig. 13. (A) Young's modulus *E* & (B) hardness as a function of Si content after thermal annealing (2 h/700 °C/air): • = as-deposited & ■ = annealed.

The evolution of the mechanical properties after the thermal annealing is presented in Fig. 13. The mechanical properties exhibited a decreasing tendency as a function of the TiO_2-rutile formation.

For instance, in the sample containing the 8.8 at.% Si, hardness declines in a lower proportion. As already reported by *Choi* et al., in these types of nanocomposites, it is well known that the oxidation resistance is progressively improved with the increasing amount of Si [4,35].

Higher silicon content (over 4.4 at.% Si) permits to limit the mechanical properties deterioration at higher temperature in an air atmosphere. According to *Steyer* et al., since the refractory amorphous matrix encapsulates the TiN nanocrystallites, it acts as an efficient oxygen diffusion barrier, which enhances the oxidation resistance [36]. It is believed that SiO_2 acts as oxygen diffusion barrier [4,36].

4. Discussion

Nanocomposites are composed of nanometric grains (<50 nm) separated by the grain boundaries (GBs). Grain boundary hardening is described by Hall-Petch relationship which is based on the dislocation pile-up mechanism.

However, as claimed firstly by *Chokshi* et al., when grain sizes are reduced down to 10–20 nm, the mechanical properties progressively decrease due to the inverse Hall-Petch effect [37]. This phenomenon is ascribed to the excessive shear deformation at GBs,

the so-called grain boundary sliding. During deformation, the nanocrystallites are obliged to displace against one another [38].

Nonetheless, by a proper materials selection and coating microstructure such as in these nanocomposites, it is possible to counteract the deformation mechanism. The mechanical behaviour is essentially determined by the GBs, since the number of atoms (volume fraction) in crystallites is comparable to those at GBs. As a consequence, the dislocation generation is impeded and the presence of hard GBs partially inhibits the grain boundary sliding mechanism. This phenomenon would explain the mechanical properties enhancement in these nanocomposites [1]. Theoretically, these nanocrystallites must exhibit random orientation with the aim of minimizing the incoherent strain and releasing the latter to the matrix. Therefore, the matrix should allow the coherent strains accommodation between the nanocrystallites. This phenomenon implies the absence of defects – i.e. voids or flaws, as well as the nanocracks deflection. In this context, a higher hardness can be achieved.

Carsley et al. proposed a hardness-crystallite size model [39] for nanostructure materials which allows to fit the experimental data with the following Eq. (1):

$$H(d) = f_c \cdot \left(H_o + \beta \cdot d^{-0.5}\right) + (1 - f_c) \cdot H_{\text{G.B.}} \quad (1)$$

Where f_c and $(1 - f_c)$ are the volume fraction of the nanocrystallites and the GBs, H_o and β are the Hall–Petch parameters, d the grain size, and $H_{\text{G.B.}}$ is the hardness of the boundary phase. This hardness model exhibits the dependence between the hardness of both phases and the fraction of atoms at the GBs. The latter determined by their thickness and the shape of nanocrystals. Hence, the model explains how it is possible to achieve the so-called strongest size when crystallite sizes are near $\approx$10–15 nm for well-consolidated materials such as PVD or PECVD thin films according to *Veprek* et al. [40]. It is believed that this maximum is determined by the optimum compromise between the two contradictory phenomena, i.e. Hall-Petch hardening and the grain boundary sliding.

In the present study, the hardness enhancement was also measured between a closer range of nanocrystallites size (8–6 nm) corresponding to Si contents within 3.5–4.4 at.%. It is well known that a further increase in Si content over the percolation threshold (p_c) – leads to the reduction in terms of phases interaction imputed to large amount of the amorphous phase. As a consequence, the nanocracks are able to propagate through the matrix, and hardness is only determined by its properties [24].

The beneficial effect of the Si addition on the oxidation resistance was reported in different studies [4,34–36]. According to *Diserens* et al., the improved oxidation resistance compared to the single nitride, is perfectly ascribed to the formation of amorphous silica which as an anti-diffusion layer [34]. Consequently, it is believed that the amorphous silica formed on the TiO_2 GBs is a passive layer which retards *O* diffusion into the nanocrystallites as well as the Ti atoms migration – up to a temperature threshold – thus preserving the TiSiN stability. In fact, by increasing the atomic percentages of Si, it is possible to proportionally enhance the oxidation resistance.

In contrast, in single-phased TiN, GBs are directly exposed to the oxygen at high temperature environments, which permit the oxygen diffusion at the GBs, hence allowing the formation of the TiO_2-rutile layer [41].

In this study, the measured properties were similar to those reported in the literature for co-sputtering and arc deposition techniques. However, the main advantage of the hybrid processing route compared to the state-of-the-art is its improved adhesion and morphology thanks to the titanium HiPIMS sputtering. Similar mechanical properties without defects (micro-droplets) such as in CAD coatings were obtained. This latter is quite interesting from the industrial point of view compared to other current techniques. An additional advantage is the use of two different target elements which avoids the alloy targets materials, thus reducing the complexity and the associated costs.

5. Conclusions

TiSiN nanocomposites were deposited by hybridizing two different magnetron sputtering techniques, i.e. HiPIMS and DC-Pulsed. The former permitted to sputter the Ti and the latter supplied the power to the silicon target, respectively. This approach allows a perfect control of the silicon content in the films. The variation of the discharge intensity on the silicon target permits the TiN nanocrystallite refinement as a function of the Si enrichment. As a consequence, TiN nanocrystallites decreased from ~41 to ~6 nm. This evolution allowed to obtain a hardness enhancement evolving from 20 ± 0.41 to 41.31 ± 2.93 GPa. Above this value, the mechanical properties remained constant closed to 35 GPa up to 8.8 at.% Si content.

In this context, the tribological properties were subsequently ruled by these mechanical properties, following the H/E ratio as reported in literature. Nonetheless, by increasing the silicon content it was possible to enhance the oxidation resistance at high temperature (700 °C) compared to single-phased TiN in an air atmosphere. As presented in this study, the sample characterized by the highest Si content (8.8 at.% Si) presented the lowest TiO_2-rutile content as well as its hardness deterioration compared to the single TiN.

The measured mechanical properties were similar to those already reported in several studies. Nevertheless, HiPIMS provides an enhanced adhesion and densification compared to cathodic arc deposition techniques. Moreover, this process is easily up-scalable since it employs the existing magnetron sputtering devices.

Acknowledgements

This work was granted by the CEA Cross-Cutting program on Advanced Materials. The authors also acknowledge Pays de Montbéliard Agglomération for its support to the study.

References

[1] Vepřek S, Reiprich S. Thin Solid Films 1995;268:64–71.
[2] Cheng YH, Browne T, Hackerman B, Meletis EI. Surf Coat Technol 2010;204:2123–9.
[3] Vepřek S, Reiprich S, Shizhi L. Appl Phys Lett 1995;66:2640–2.
[4] Choi JB, Cho K, Lee MH, Kim KH. Thin Solid Films 2004;447–448:365–70.
[5] Bendavid A, Martin PJ, Cairney J, Hoffman M, Fischer-Cripps AC. Appl Phys A 2005;81:151–8.
[6] Vepřek S, Vepřek-Heijman MGJ, Karvankova P, Prochazka J. Thin Solid Films 2005;476:1–29.
[7] Rebouta L, Tavares CJ, Aimo R, Wang Z, Pischow K, Alves E, et al. Surf Coat Technol 2000;133–134:234–9.
[8] Vaz F, Rebouta L, Goudeau Ph, Girardeau T, Pacaud J, Riviére JP, et al. Surf Coat Technol 2001;146–147:274–9.
[9] Schmitt T, Steyer P, Fontaine J, Mary N, Esnouf C, O'Sullivan M, et al. Surf Coat Technol 2012;213:117–25.
[10] Gudmundsson JT, Brenning N, Lundin D, Helmersson U. J Vac Sci Technol A 2012;30:030801.
[11] Ehiasarian AP, Wen JG, Petrov I. J Appl Phys 2007;101:05430.
[12] Flick A, Larsson T, Sjölén J, Karlsson L, Hultman L. Surf Coat Technol 2005;200:1535–42.
[13] Sanchette F, Ducros C, Schmitt T, Steyer P, Billard A. Surf Coat Technol 2011;205:5444–53.
[14] Schuster F, Lomello F. J Appl Phys Conf Ser 2013;429:012054.
[15] Bobzin K, Bagcivan N, Immich P, Bolz S, Alami J, Cremer R. J Mater Process Technol 2009;209:165–70.
[16] Paulitsch J, Schenkel M, Zufraβ Th, Mayrhofer PH, Münz WD. Thin Solid Films 2010;518:5558–64.

[17] Greczynski G, Lu J, Johansson M, Jensen J, Petrov I, Greene JE, et al. Vacuum 2012;86:1036–40.
[18] Greczynski G, Lu J, Johansson MP, Jensen J, Petrov I, Greene JE, et al. Surf Coat Technol 2012;206:4202–11.
[19] Zhang S, Bui XL, Jiang J, Li X. Surf Coat Technol 2005;198:206–11.
[20] Oliver WC, Pharr GM. J Mater Res 1992;7:1564–80.
[21] Bückle H. Metall Rev 1959;4:49–100.
[22] Cleymand F, Ferry O, Kouitat R, Billard A, Von Stebut J. Surf Coat Technol 2005;200:890–3.
[23] Ehiasarian AP, Vetushka A, Aranda Gonzalvo Y, Sáfrán G, Székely L, Barba PB. J Appl Phys 2011;109:104314.
[24] Patscheider J, Zehnder T, Desirens M. Surf Coat Technol 2001;146–147: 201–8.
[25] Pelleg J, Zevin LZ, Lungo S, Croitoru N. Thin Solid Films 1991;197:117–28.
[26] Martin PJ, Bendavid A. Surf Coat Technol 2003;163–164:245–50.
[27] Vepřek S. Pure Appl Chem 1996;68:1023–7.
[28] Lomello F, Arab Pour Yazdi M, Sanchette F, Schuster F, Tabarant M, Billard A. Surf Coat Technol 2014;238:216–22.
[29] Kim SH, Jang JW, Kang SS, Kim KH. J Mater Process Technol 2002;130–131: 283–8.
[30] Ma S, Procházka J, Karvánková P, Ma Q, Niu X, Wang X, et al. Surf Coat Technol 2005;194:143–8.
[31] Ducros C, Sanchette F. Surf Coat Technol 2006;201:1045–52.
[32] Leyland A, Matthews A. Surf Coat Technol 2004;177–178:317–24.
[33] Lomello F, Sanchette F, Schuster F, Tabarant M, Billard A. Surf Coat Technol 2013;224:77–81.
[34] Diserens M, Patscheider J, Lévy F. Surf Coat Technol 1999;120–121:158–65.
[35] Vaz F, Rebouta L, Goudeau P, Pacaud J, Garem H, Rivière JP, et al. Surf Coat Technol 2000;133–134:307–13.
[36] Steyer P, Pilloud D, Pierson JF, Millet JP, Charnay M, Stauder B, et al. Surf Coat Technol 2006;201:4158–62.
[37] Choksi AH, Rosen A, Karch J, Gleiter H. Scr Metall 1989;23:1679–84.
[38] Zhang S, Wang HL, Ong SE, Sun D, Bui XL. Plasma Process Polym 2007;4: 219–28.
[39] Carsley JE, Ning J, Milligan WW, Hackney SA, Aifantis EC. Nanostruct Mater 1995;5:441–8.
[40] Vepřek S, Vepřek-Heijman MGJ. Thin Solid Films 2012;522:274–82.
[41] Ichimura H, Kawana A. J Mater Res 1993;8:1093–100.